


Numerical Investigation on Flame Stabilization in DLR Hydrogen Supersonic Combustor with Strut Injection

Kun Wu, Peng Zhang, Wei Yao & Xuejun Fan

To cite this article: Kun Wu, Peng Zhang, Wei Yao & Xuejun Fan (2017): Numerical Investigation on Flame Stabilization in DLR Hydrogen Supersonic Combustor with Strut Injection, Combustion Science and Technology, DOI: [10.1080/00102202.2017.1365847](https://doi.org/10.1080/00102202.2017.1365847)


To link to this article: <http://dx.doi.org/10.1080/00102202.2017.1365847>

 View supplementary material [↗](#)

 Accepted author version posted online: 18 Aug 2017.
Published online: 18 Aug 2017.

 Submit your article to this journal [↗](#)

 Article views: 65

 View related articles [↗](#)

 View Crossmark data [↗](#)



Numerical Investigation on Flame Stabilization in DLR Hydrogen Supersonic Combustor with Strut Injection

Kun Wu^{a,b,c}, Peng Zhang^b, Wei Yao^{a,c}, and Xuejun Fan^{a,c}

^aState Key Laboratory of High Temperature Gas Dynamics, Chinese Academy of Sciences, Beijing, People's Republic of China; ^bDepartment of Mechanical Engineering, Hong Kong Polytechnic University, Hong Kong; ^cSchool of Engineering Sciences, University of Chinese Academy of Sciences, Beijing, People's Republic of China

ABSTRACT

Flame stabilization in the DLR hydrogen supersonic combustor with strut injection was numerically investigated by using an in-house large eddy simulation code developed on the OpenFoam platform. To facilitate the comparison and analysis of various hydrogen oxidation mechanisms with different levels of mechanism reduction, the proposed 2D calculation model was validated against both the 3D simulation and the experimental data. The results show that the 2D model can capture the DLR flow and combustion characteristics with satisfactorily quantitative accuracy and significantly less computational load. By virtue of the flow visualization and the analyses of species evolution and heat release, the supersonic combustion in the DLR combustor can be divided into three stages along the streamwise direction: the induction stage where ignition occurs and active radicals are produced, the transition stage through which radicals are advected to the downstream, and the intense combustion stage where most heat release occurs. Furthermore, the sensitivity analysis of key reaction steps identifies the important role of chain carrying and heat release reactions in numerically reproducing the three-stage combustion stabilization mode in the DLR combustor.

ARTICLE HISTORY

Received 23 March 2017
Revised 18 July 2017
Accepted 6 August 2017

KEYWORDS

Detailed hydrogen oxidation mechanism; DLR; Flame stabilization; Sensitivity analysis; Supersonic combustion


Introduction

With the increasing interest in high-speed reusable space vehicles, much effort has been devoted to the development of hypersonic air-breathing propulsion systems (Bertin and Cummings, 2003). Due to its promising performance at flight Mach numbers higher than seven, the supersonic ramjet (also known as scramjet) fueled with hydrogen has been extensively studied over the past decades (Cecere et al., 2011). Compared with those fueled with liquid hydrocarbons, employing hydrogen in scramjets mitigates the technical difficulties of atomizing, vaporizing, mixing, and igniting liquid fuels in a supersonic combustor flow that has a short residence time of a millisecond or less (Ben-Yakar et al., 2006).

Whereas it is technically challenging and financially demanding to reproduce realistic flight conditions in ground test facilities, computational fluid dynamics (CFD) have been widely used as an alternative tool in scramjet design and analysis (Fureby et al., 2011; Li et al., 2014a, 2014b). Nevertheless, due to the technical difficulties of performing high-accuracy measurements in the harsh supersonic flow field containing shock waves,

CONTACT Peng Zhang  pengzhang.zhang@polyu.edu.hk 

Color versions of one or more of the figures in the article can be found online at www.tandfonline.com/gcst.

 Supplemental data for this article can be accessed on the [publisher's website](#).

© 2017 Taylor & Francis

boundary layers, and combustion, the wall static pressures are often merely available experimental data and found inadequate for validating CFD results.

The Institute of Chemical Propulsion of the German Aerospace Center carried out various measurements on its hydrogen supersonic model combustor with strut fuel injection (Waidmann et al., 1994; referred to as DLR combustor hereinafter). Several features of the DLR combustor make it particularly suitable for validating CFD results. First, compared with other existing supersonic combustors, the DLR combustor is a small-scale laboratory model and requires significantly fewer grids for numerical discretization, especially for that in large eddy simulation (LES). Second, the DLR combustor is fueled with hydrogen and therefore substantially reduces the computational complexity and uncertainty of chemical reaction mechanisms of hydrocarbon fuels. Finally, systematic and comprehensive measurements were conducted to the DLR combustor under both cold and reacting flow conditions. The rich measurement data include the transverse velocity profiles measured by using laser Doppler velocimetry, the static temperature profiles by using coherent anti-Stokes Raman spectroscopy at streamwise locations, the axial velocity along the combustor centerline, and the static pressures along the centerline and the lower wall. The shadowgraphs of the cold and reactive flow fields are also available for visualizing the shock waves in the combustor.

Numerical studies on the DLR hydrogen combustor by using either Reynolds averaged Navier–Stokes (RANS) or LES have been comprehensively tabulated in supporting material (Supplementary material) and will be briefly summarized here. A 2D RANS calculation of Oevermann (2000) shows agreement with the experimental data, but the calculated static temperature profiles in the far downstream of the strut overshoot the experimental data, possibly because the effective overall equivalence ratio in his calculation is higher than the experimental value. Potturi and Edwards (2012) found that their RANS calculation yields better predictions to the velocity profiles but worse time-averaged static temperature than their LES/RANS simulation.

To analyze and compare previous LES studies on the DLR supersonic combustor, several important aspects, such as high-order numerical algorithm, turbulence-chemistry interaction modeling, and hydrogen oxidation mechanism, must be taken into account (Fureby, 2012). By using a predictor-corrector scheme with total variational diminishing (TVD) preserving flux reconstruction algorithm, Génin and Menon (2010b) found that their LES can resolve the shock waves and the turbulent eddies in the DLR combustor with minimized numerical dissipation, and pointed out that the Kelvin–Helmholtz instability generated in the early stage of the shear layer development (originating from the strut tail) leads to the formation of 2D spanwise vortices. Berglund and Fureby (2007) and Fureby et al. (2014) used finite volume-based monotonicity preserving flux reconstruction schemes and found that the flow field has some 2D large-scale flow structures.

Waidmann et al. (1994) indicated that the non-premixed combustion in the DLR combustor belongs to either the corrugated flamelet regime or the distributed reaction zone regime. Consequently, flamelet, finite-rate chemistry, and quasi-laminar chemistry models have been adopted in the LES or LES/RANS studies of DLR. By using a quasi-laminar chemistry model, Génin and Menon (2010b) found that the DLR combustor flame is embedded in a recirculation region located in the far downstream of the strut. The LES/RANS study of Potturi and Edwards (2012), employing the same model, found a lifted flame anchored at the maximum penetration point of the hydrogen jet. In Berglund

and Fureby's (2007) LES study with one- and two-equation flamelet models, the DLR combustor flame embedded in the strut wake can be divided into three zones, such as the induction zone, the translational zone, and the turbulent flame zone. Fureby et al. (2014) found that the finite-rate PaSR model produces better predictions in both the time-averaged axial velocity and the temperature profiles than the flamelet model. Huang et al. (2015) also adopted the PaSR model and proposed that the auto-ignition plays an important role in flame stabilization and lift-off.

The most prevalent hydrogen oxidation mechanism for the supersonic combustion simulations is Jachimowski's (1988) one consisting of nine species and 20 reactions (referred to as the J-9S-20R mechanism hereinafter). Because of its relatively large size, the full version of the J-9S-20R mechanism was only used in the recent LES/RANS study of Potturi and Edwards (2012, 2014). Based on the J-9S-20R mechanism and invoking the quasi-steady state assumptions to remove the intermediate species HO_2 and H_2O_2 , Eklund et al. (1990) derived a 7-species and 7-reaction reduced mechanism (E-7S-7R), which however contains a non-elementary reaction, $\text{H}_2 + \text{O}_2 \rightarrow 2\text{OH}$, to mimic the chain initiation. Both the J-9S-20R and E-7S-7R mechanisms were adopted in the LES/RANS study of Potturi and Edwards (2012), but the predicted flame is detached from the strut, in contradiction with the experimental observation. By adjusting the rate constants in the E-7S-7R mechanism to fit the experiment, Davidenko and Magre (2003) obtained a modified version (D-7S-7R). Another 7-species and 7-reaction mechanism proposed by Baurle et al. (1994; B-7S-7R) was adopted by Génin and Menon (2010b) in their LES study of DLR. The deficiencies of reduced mechanisms were also observed: Fureby et al. (2014) found Rogers and Chinitz's (1983) two-step mechanism is incapable of predicting the static temperature profiles compared with the D-7S-7R mechanism; Berglund and Fureby (2007) found that the one-step mechanism of Marinov et al. (1995; M-3S-1R) results in too early ignition, compared with the two-step and the D-7S-7R mechanisms.

It is noted that these worthy numerical studies of the DLR combustion were mainly focused on validating numerical algorithms and combustion models. The understanding of the flame stabilization mechanism of the DLR combustor is still far from being satisfactory, and the role of the chemical reaction mechanism in accurately predicting the flame characteristics has not been sufficiently clarified from the viewpoint of chemical kinetics. Specifically, the experiment shows that the attached DLR flame extends from the relatively low-speed recirculation zone in the immediately downstream of the strut to the farther downstream where the local flow velocities are substantially high. The failures of the over-simplified one-step or two-step reduced mechanisms in predicting this flame feature suggest that the DLR flame cannot be described by using either the thermal theory or simple fuel chemistry. Instead, the flame in both low- and high-speed regions must be controlled by different chemical species and elementary reactions.

Based on the above considerations, we formulated the present LES study to understand the flame stabilization by using the PaSR combustion model of Karlsson (1995) and the state-of-the-art hydrogen combustion mechanism established by Burke et al. (2011; B-9S-19R). The B-9S-19R mechanism has been validated against many experimental data on various flames over wide ranges of temperature and pressure. The widely-used one-step mechanism, M-3S-1R, and the E-7S-7R mechanism were also used in the study for comparison. To facilitate the sensitivity analysis of these mechanisms in predicting the

flame characteristics, a 2D calculation model of the DLR combustor was proposed and validated against the experimental data and the 3D simulations.

We shall first present the numerical methodology in the following section, including the sub-grid turbulence and combustion models, the 2D and 3D computational models and grids of the DLR combustor, then the grid convergence study. The 2D calculation will be validated against both the 3D simulation and the experimental data in the third section. The flame stabilization mechanism in the DLR combustor will be analyzed in the fourth section, followed by the sensitivity analysis for clarifying the role of key chain reactions in influencing the flame stabilization in the final section.

Numerical methodology

Governing equations and numerical algorithm

By performing Favre filtering to the continuity, momentum, energy, and species equations of compressible reacting flows, we obtained:

$$\frac{\partial \bar{\rho}}{\partial t} + \frac{\partial \bar{\rho} \tilde{u}_i}{\partial x_i} = 0 \quad (1)$$

$$\frac{\partial \bar{\rho} \tilde{u}_i}{\partial t} + \frac{\partial}{\partial x_j} \left[\bar{\rho} \tilde{u}_i \tilde{u}_j + \bar{p} \delta_{ij} - \bar{\tau}_{ij} + \tau_{ij}^{sgs} \right] = 0 \quad (2)$$

$$\frac{\partial \bar{\rho} \tilde{E}}{\partial t} + \frac{\partial}{\partial x_i} \left[(\bar{\rho} \tilde{E} + \bar{p}) \tilde{u}_i + \bar{q}_i - \tilde{u}_j \bar{\tau}_{ij} + H_i^{sgs} + \sigma_i^{sgs} \right] = \bar{Q} \quad (3)$$

$$\frac{\partial \bar{\rho} \tilde{Y}_k}{\partial t} + \frac{\partial \bar{\rho} \tilde{u}_i \tilde{Y}_k}{\partial x_i} + \frac{\partial}{\partial x_i} \left[-\bar{\rho} D_{km} \frac{\partial \tilde{Y}_k}{\partial x_i} + \Upsilon_{i,k}^{sgs} + \theta_{i,k}^{sgs} \right] = \bar{\omega}_k k = 1, \dots, N_s \quad (4)$$

where “ $\bar{\cdot}$ ” and “ $\tilde{\cdot}$ ” denote spatial and Favre filtering, $u_i (i = 1, 2, 3)$ is the velocity vector in Cartesian coordinates, ρ the density, p the pressure, τ_{ij} the viscous stress tensor, q_i the heat flux vector, $E = h_s - p/\rho + u_i u_i/2$ the total energy and h_s the sensible enthalpy, Y_k the mass fraction of the k^{th} species, D_{km} the binary mass diffusivity of the k^{th} and m^{th} species, $\dot{\omega}_k$ the production rate of the k^{th} species, \bar{Q} the heat release due to combustion, and N_s the total number of species. Sutherland’s law is used to calculate the viscosities of species, based on which the thermal conductivities and mass diffusivities are obtained by assuming the constant Prandtl number ($Pr = 0.7$) and Schmidt number ($Sc = 0.7$). Thermodynamic data are obtained from the NIST-JANAF thermophysical database (Chase, 1974). The equation of state for perfect gas is used and its filtered version is given by $\bar{p} = \bar{\rho} R \tilde{T}$, where

T is the temperature, $R = \sum_{k=1}^{N_s} Y_k R_u / MW_k$ the mixture gas constant, MW_k the species

molecular weight, and R_u the universal gas constant. All of the sub-grid scale terms are denoted by the superscript “sgs” and their closure will be described shortly in the following subsection.

An in-house code, AstroFoam, which was developed based on the OpenFoam platform, was used in the present study. AstroFoam has been used in the previous studies for simulating multicomponent supersonic flows and can capture shock waves and resolve turbulent eddies

with high resolutions (Li et al., 2016a, 2016b). AstroForm adopts the second-order, semi-discrete, non-staggered, central-upwind, Kurganov and Tadmor (KT) scheme (Kurganov and Tadmor, 2000), which has been implemented in the OpenFoam framework (Greenshields et al., 2009) in order to capture the flow discontinuities (e.g., shock waves) with non-oscillatory and low-dissipation features. The high-order reconstruction of all convective fluxes at faces (fluxes limiter-based) using a second-order TVD-type scheme is believed to have nominal second-order accuracy in the spatial integration. The adopted semi-implicit Crank–Nicholson scheme (Baba-Ahmadi and Tabor, 2009) is of second-order accuracy in the time integration. Although it is noted that higher-order spatial integration schemes have been widely used in the LES of low-speed turbulent flow, the numerical schemes adopted by Astroform is the balance of computational expense and accuracy.

Sub-grid models

Given the eddy viscosity ν_t , the sub-grid stress, τ_{ij} , is calculated by:

$$\tau_{ij}^{sgs} = -2\bar{\rho}\nu_t \left(\tilde{S}_{ij} - \frac{1}{3}\tilde{S}_{kk}\delta_{ij} \right) + \frac{2}{3}k^{sgs}\delta_{ij} \quad (5)$$

where

$$\tilde{S}_{ij} = \frac{1}{2} \left(\frac{\partial \tilde{u}_i}{\partial x_j} + \frac{\partial \tilde{u}_j}{\partial x_i} \right), k^{sgs} = (1/2)[\widetilde{u_k u_k} - \tilde{u}_k \tilde{u}_k] \quad (6)$$

H_i^{sgs} and σ_i^{sgs} in Eq. (3) are modeled together by:

$$H_i^{sgs} + \sigma_i^{sgs} = -\frac{\bar{\rho}\nu_t}{Pr_t} \left(\frac{\partial \tilde{h}_s}{\partial x_i} + \tilde{u}_j \frac{\partial \tilde{u}_i}{\partial x_j} + \frac{\partial k^{sgs}}{\partial x_i} \right) \quad (7)$$

The sub-grid species fluxes, $\Upsilon_{i,k}^{sgs}$, is given by:

$$\Upsilon_{i,k}^{sgs} = -\bar{\rho} \frac{\nu_t}{Sc_t} \frac{\partial \tilde{Y}_k}{\partial x_i} \quad (8)$$

in which Sc_t is set to be 0.9. The SGS species diffusive fluxes, $\theta_{i,k}^{sgs}$, has been found insignificant in the previous studies on supersonic flow simulations (Génin and Menon, 2010a; Pino Martín et al., 2000) and will be neglected in the present simulation.

The characteristic length and velocity scales are related to the filter width $\bar{\Delta}$ and sub-grid kinetic energy, k^{sgs} , respectively. Consequently, the eddy viscosity is defined by $\nu_t = c_v \bar{\Delta} \sqrt{k^{sgs}}$ where c_v equals to 0.094, k^{sgs} is determined by solving its transport equation (Chakravarthy and Menon, 2001; Yoshizawa, 1986):

$$\frac{\partial \bar{\rho} k^{sgs}}{\partial t} + \frac{\partial \bar{\rho} \tilde{u}_j k^{sgs}}{\partial x_j} = \frac{\partial}{\partial x_j} \left[\bar{\rho} \left(\frac{\nu_t}{Pr_t} + \nu \right) \frac{\partial k^{sgs}}{\partial x_j} \right] - \tau_{ij}^{sgs} \frac{\partial u_j}{\partial x_i} - C_\epsilon \frac{\bar{\rho} (k^{sgs})^{3/2}}{\bar{\Delta}} \quad (9)$$

where $C_\epsilon = 1.048$ is a model constant and $Pr_t = 0.72$ in the present study. Fureby et al. (1997) compared various SGS models in supersonic wall-bounded flows and found that

the above one-equation model exceeds the zero-equation models in modeling flow transition and unsteadiness.

The present study adopts the finite-rate PaSR model of Karlsson (1995), which has been widely used in high speed turbulent combustion. In the PaSR model, each LES cell is divided into the fine structures in which mixing and reaction take place, and the surrounding, which is dominated by large-scale flow structures. The mixing and reaction in the fine structures occur sequentially and are characterized by the time scales τ_m and τ_c , respectively. The smallest scale of relevance to the subgrid mixing is the Kolmogorov scale, and thus the mixing characteristic time is assumed to be the same order of the Kolmogorov time scale, yielding $\tau_m \sim \tau_K = (v_{eff}/\epsilon)^{1/2}$ where v_{eff} is the turbulent kinematic viscosity and ϵ is the viscous dissipation rate. The turbulent kinetic energy k field affects the mixing time scale through v_{eff} and ϵ . The characteristic time of chemical reaction is expressed as $\tau_c = \delta_u/s_u$, where δ_u and s_u are the thickness and speed of the laminar flame.

The reacting volume fraction κ is defined as the ratio of the volume swept by the reacting fine structures and that by the mixing and reacting structures and can be estimated by $\kappa = \tau_c/(\tau_m + \tau_c)$. Consequently, the filtered reaction rate is estimated by $\overline{\dot{\omega}_i(\rho, T, Y_i)} \approx \kappa \dot{\omega}_i(\bar{\rho}, \bar{T}, \bar{Y}_i)$, in which $\dot{\omega}_i(\bar{\rho}, \bar{T}, \bar{Y}_i)$ is the reaction rate based on the filtered physical quantities and κ is used to account for the strengthening or attenuating effects of turbulence to chemical reaction.

Regardless of its relatively simple form, the PaSR model has been used in many previous studies for not only practical calculations but also understanding physical processes. For example, Nordin–Bates et al. (2017) investigated detailed physical processes occurring in the HyShot II combustor and found that supersonic combustion in the combustor is a combination of auto-ignition and non-premixed flame regions and self-ignition fronts. Another example is that Fulton et al. (2016) employed the PaSR model to study the turbulence-chemistry interaction in a model scramjet.

Computational specifications

The schematic of the DLR combustor is shown in Figure 1 and the experimental parameters are given in Table 1. The coordinates \hat{x} and \hat{y} in the streamwise and transverse directions are respectively normalized using the characteristic length L and height H . $Ma =$

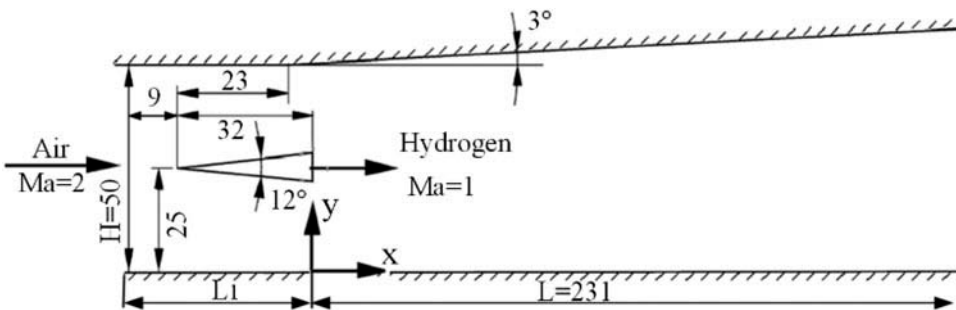


Figure 1. Schematic of the DLR combustor (unit in mm).

Table 1. Experimental parameters of the DLR combustor.

Variables	Ma	U (m/s)	P (MPa)	T (K)	Y_{O_2}	Y_{N_2}	Y_{H_2O}	Y_{H_2}
Air	2.0	730	0.1	340	0.232	0.736	0.032	0
H ₂	1.0	1200	0.1	240	0	0	0	1.0

2 air flow enters the combustor, whose entrance is 50 mm in height and 40 mm in width, and whose upper wall is slightly divergent by 3° from $\hat{x} = -0.039$ to compensate for the boundary layer. A wedge-shaped strut that is 32 mm in length and has a half divergent angle of 6° is installed along the combustor centerline, with its base located at $\hat{x} = 0$. Sonic hydrogen flow is injected through an array of 15 evenly-spaced fuel orifices on the base of the strut. The diameter of each fuel orifice is 1.0 mm and the distance between two adjacent orifices is 2.4 mm.

In the present study, two types of computational models were adopted. The 2D model is two-dimensional in geometry, as shown in Figure 2, where the fuel orifice is replaced by a 2D slot-like injection. In order to keep the overall air/fuel flow rate the same as that of the experiment while retaining the local flow structure near the fuel injector, a periodic injection scheme is specified at the fuel injector. As shown in Figure 2, the 2D slot is evenly divided into 52 portions and sonic hydrogen flow is injected from the other two portions, the others being treated as solid walls. Such an injection scheme produces the overall equivalence ratio in the present 2D calculation, the same as the experimental one (0.034), which is however not reproduced in the 2D RANS calculation of Oevermann (2000). In the present study, a block structured hexahedral grid is employed for all mesh generations. The mesh used in the 2D calculations is shown in Figure 2, in which the grid is refined near the fuel injector and the flow shear layers. Over the 6.7-mm-wide strut (in the Y direction) 150 grids are distributed. The average and maximum cell sizes in the mixing region are 0.08 mm and 0.15 mm, respectively.

For the 3D simulation, one fuel injector is enclosed with periodic boundaries in the spanwise directions. Such a 3D geometry has been used in previous studies (Génin and Menon, 2010b; Gong et al., 2017). The 3D computational domain is 2.4 mm in width, which is the distance between two adjacent fuel injectors. For the 3D mesh, the number of grid cells over the strut is 115 and the regions near the fuel orifice and the upper/lower shear layer are also refined, as shown in Figure 3. The average and maximum cell sizes in the mixing region are 0.08 mm and 0.2 mm, respectively. In the spanwise direction (Z direction) 24 grid points

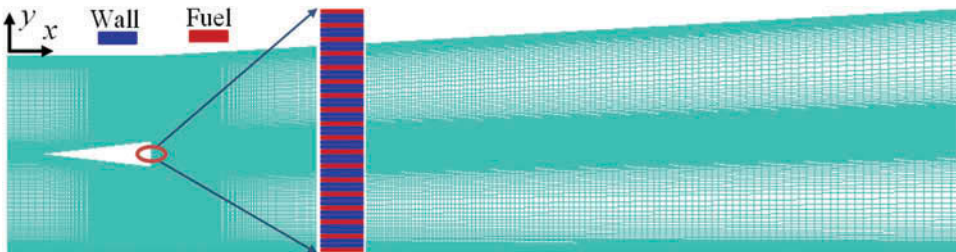


Figure 2. Schematic of the computational domain and the mesh (one sixth of the grid is shown for better visualization) for the 2D calculation; The periodic injection scheme is shown in the enlarged subfigure.

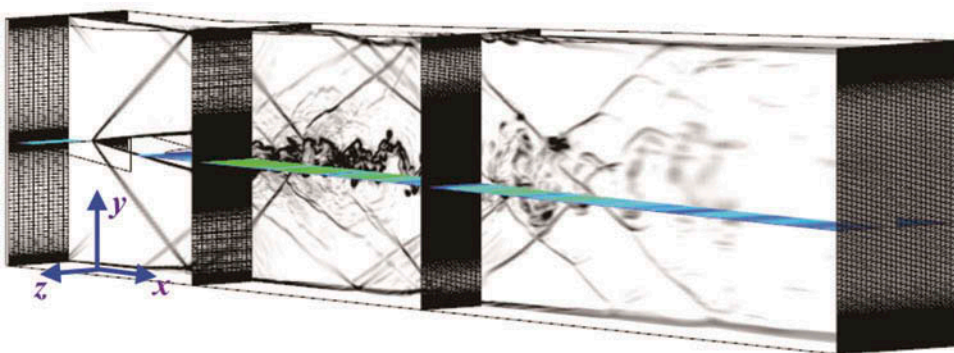


Figure 3. Computational domain with the density gradient on the center plane and the meshes on the streamwise planes for the 3D non-reacting flow simulation.

are distributed. The minimum mesh spacing at all solid walls in both 2D and 3D simulation is 5×10^{-3} mm leading to $Y^+ < 1$.

In a grid convergence study of the 2D calculation, three meshes of about 0.19, 0.27, and 0.52 million grid cells were used. Two 3D meshes of 3.16 and 5.90 million grid cells were used for the grid convergence study. The finer 3D mesh has about 0.25 million cells in the X-Y plane, which are comparable to the moderately refined 2D mesh with 0.27 million grid cells. For both 2D and 3D grid convergence studies, the mesh refine was mainly conducted in the streamwise direction and the grids in the other direction(s) were adjusted to meet the LES mesh requirement.

At the combustor inlet, inflow boundary conditions for all the variables other than velocity are specified, and the velocity mean profiles are superimposed with sinusoidal perturbation velocities with 5% amplitude of the mean values. The sub-grid kinetic energy k at the inflow boundary corresponds to a turbulence level of 0.5% for the air and 5% for the hydrogen jet. The supersonic outflow boundary condition is specified at the combustor exit.

At the solid walls, k is specified as zero. Because of the sufficient grid points near the walls with the size of the first layer being 5×10^{-6} m ($Y^+ < 1$), the damping function of Balaras et al. (1996) was used to ensure the correct limiting behavior of turbulent viscosity in the viscous layer. The damping function method was also discussed by Fureby et al. (2004) in detail. Because the previous studies have shown that the wall effect can be neglected, slip wall was employed in the DLR simulations of Oevermann (2000), Genin and Menon (2010b), Huang et al. (2015), and Gong et al. (2017). In consideration of this, the present treatment of wall turbulence is physically justifiable and believed to cause negligible influence on the results.

The initial condition for the cold flow simulation is given by the main inflow throughout the combustor and that for the reacting flow simulation is given by the fully developed non-reacting flow. The integration time step is approximately 5.0×10^{-9} s as the result of a maximum Courant–Friedrich–Lewy number of 0.6.

In the present study, the flow-through time is defined as $t_f = L/U_\infty \approx 3 \times 10^{-4}$ s with U_∞ being the air inflow velocity. The 3D cold flow simulation runs totally for $11t_f$, including $3t_f$ to reach the statistically steady state and $8t_f$ for collecting time-averaged data. For 2D cold flow calculation with the total simulation time of $8t_f$, $2t_f$ is needed for reaching a statistically steady

state and $6t_f$ for statistical data collection. For 2D reacting flow calculations, a longer time of $10t_f$ is needed to obtain statistically steady state flow field and collecting the time-averaged data. To facilitate the following discussion, the pressure, temperature, and velocity are normalized by $\hat{p} = p/p_\infty$, $\hat{T} = T/T_\infty$ and $\hat{u}_i = u_i/U_\infty$ in which the air inflow parameters are selected as reference. Furthermore, the heat release rate dQ is normalized by $C_p T$ where C_p is constant-pressure specific heat.

The present simulations were performed on 60 CPUs of TIANHE-1 super-computer center in the National Supercomputer Center in Tianjin. For the non-reacting flow, a typical run of 3D simulation cost about 20,160 CPU-hours and that of 2D calculation cost only one eighth. Because a longer flow-through time was needed for statistical data collection, the 2D reacting flow calculation cost nearly 17,280 CPU-hours for a typical run.

Grid independence analysis

Considering most of the present simulations were conducted on 2D computational model, we carried out the 2D non-reactive flow calculations by using three meshes consisting of 0.19, 0.27, and 0.52 million grids cells, respectively. It can be seen from Figure 4a that all of the meshes generate the same trend of the pressure distribution along the combustor centerline. Although minor differences were found for the first and third pressure peaks, which are caused by the interaction of shock waves in the combustor, the locations of the turning points on the pressure distribution are almost identical, implying that all the meshes can accurately capture the shock waves in the combustor. Consequently, the medium-size grid with 0.27 million cells, as a balance of computational cost and accuracy, was used in the simulations to be elaborated in the following section. Within the 3D grid convergence study, it can be seen from Figure 4b that only a minor difference arises when the mesh grids are almost doubled. The slight discrepancy near $\hat{x} = 0.4$ may be caused by the more meticulous resolved vortex-shock interaction with the finer mesh. In consideration of this, the results from the finer 3D mesh will be used when compared with 2D calculations.

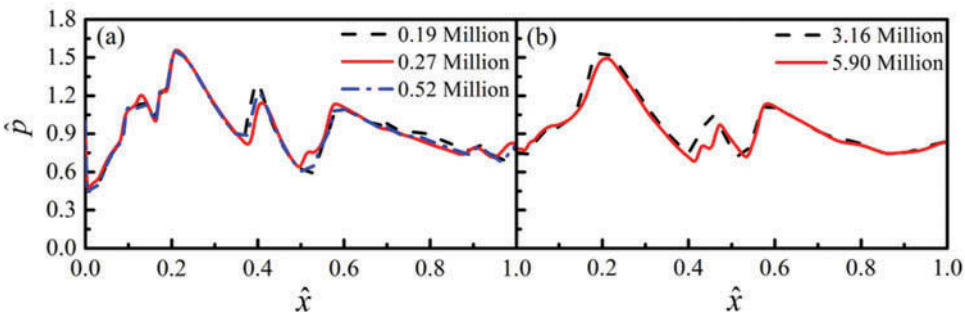


Figure 4. Grid independence analysis on (a) the 2D non-reacting flow calculation and (b) the 3D non-reacting flow simulation.

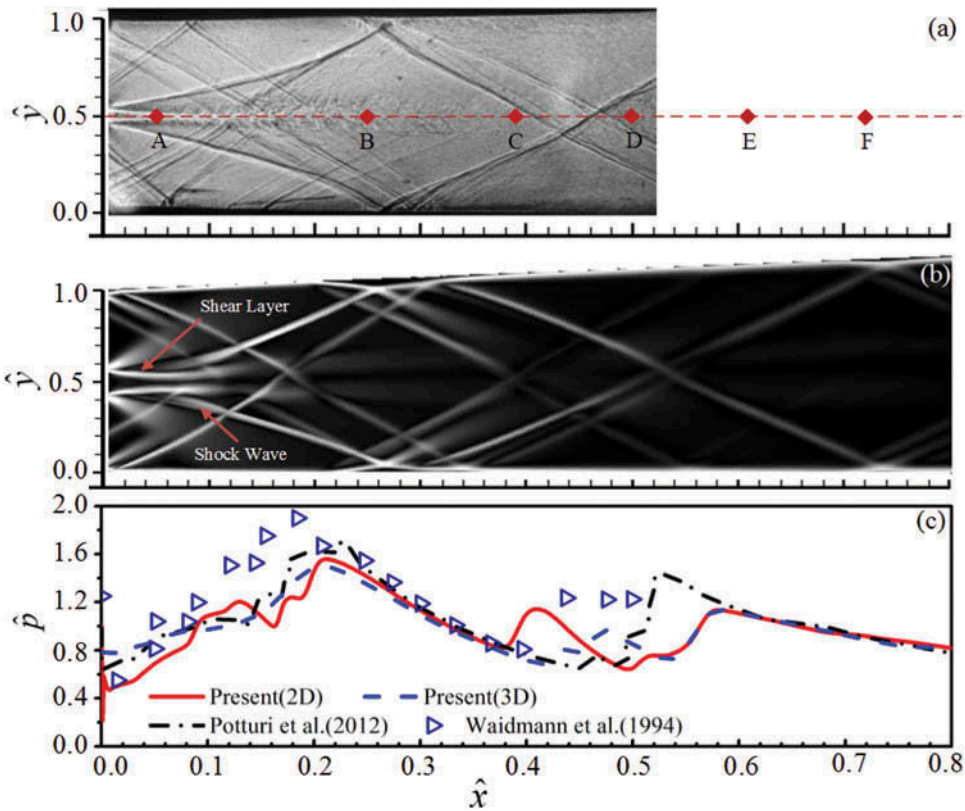


Figure 5. (a) Experimental shadowgraph from Waidmann et al. (1994). (b) Time-averaged density gradient field from the 2D non-reacting flow calculation. (c) Time-averaged pressure distribution along the combustor centerline from the 2D and 3D calculations in comparison with the LES/RANS results of Potturi and Edwards (2012).

Experimental validation

Validation of non-reacting flow simulation

To describe the flow field in the combustor, the experimental shadow graph is shown in Figure 5a; the time-averaged density gradient field from the present 2D calculation is also presented in Figure 5b for comparison. To facilitate the following discussion, a series of locations where experimental measurements were conducted are indicated by $\hat{x}_A = 0.048$, $\hat{x}_B = 0.251$, $\hat{x}_C = 0.390$, $\hat{x}_D = 0.498$, $\hat{x}_E = 0.606$, and $\hat{x}_F = 0.719$. It is seen that the overall shock-wave-filled flow field is accurately reproduced by the 2D calculation. Specifically, two oblique shock waves originating symmetrically from the leading edge of the wedge-shaped strut reflect from the upper and lower walls, leaving two small separation bubbles at $\hat{x} = 0.005$. Because of the slight divergence of the upper wall, the two reflected shock waves intersect with each other at $\hat{y} = 0.580$, which is slightly above the centerline of the combustion chamber. The flow divergence at the rear corners of the strut leads to two expansion fans. The shear layers formed along the strut walls separate and bend to the combustor centerline owing to the low pressure in the wake flow.

For quantitative validation, the 2D calculation is compared with the 3D simulation and the experimental data for the pressure distribution along the combustor centerline, as shown in Figure 5c. The LES/RANS result of Potturi and Edwards (2012) is also shown in the figure for comparison. It is seen that the present 2D calculation produces overall good predictions to the pressure distribution, particularly to its peak values and locations. Regardless of that the 2D calculation under-predicts the pressure peak around $\hat{x} = 0.185$ by 15.5% (compared with the 14.9% under-prediction by Potturi and Edwards [2012]), it captures the location of the third pressure rise around $\hat{x} \approx 0.400$. The LES/RANS simulation of Potturi and Edwards (2012) predicts a slight pressure rise at $\hat{x} = 0.430$ but a significant one in the downstream, which is not seen in the experiment.

Further comparison was carried out for the streamwise velocity profiles at four different locations, as shown in Figure 6. At location A, the velocity profile of the 3D simulation manifests two crests, which are however absent in the present 2D calculation. It should be noted that both the present 3D and Potturi and Edwards's (2012) simulations overshoot the velocity at location A. At the other three locations (B, C, and F), all of the simulations show good agreement with the experimental data, substantiating that the present 2D model can retain the 2D characteristics of the DLR combustor flow field in the downstream sufficiently away from the strut and the fuel injector. In Figure 7, the streamwise

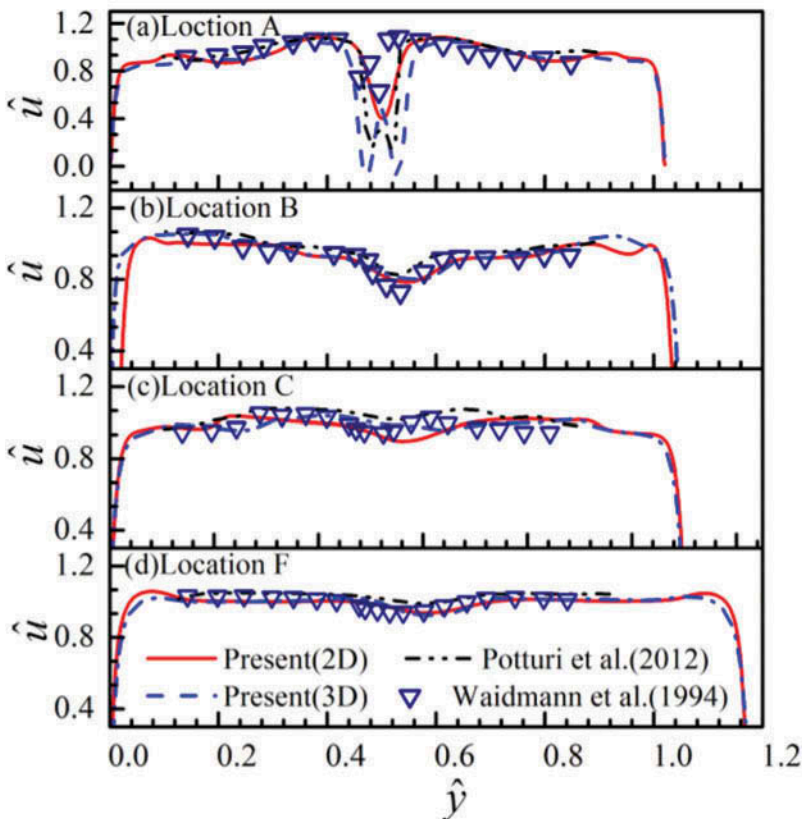


Figure 6. Time-averaged velocity profiles of non-reacting flow at four streamwise locations.

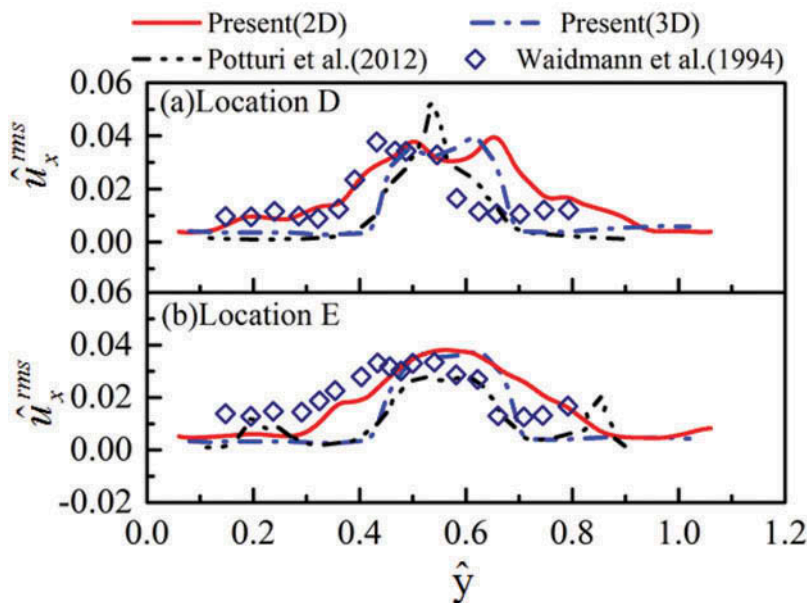


Figure 7. Streamwise velocity fluctuation profiles at two streamwise locations in the non-reacting flow.

velocity fluctuation profiles for the 2D non-reacting calculation are shown along with experimental data and the 3D simulation results. It is seen that the 2D calculation reproduces a better trend of the turbulence fluctuations along the transverse direction compared with the previous studies, further verifying the applicability of the present 2D model in the simulation of the DLR combustor.

Validation of reacting flow simulation

The experimental shadowgraph for the reacting flow is shown in [Figure 8a](#); the time-averaged density gradient field from the 2D calculation is also presented in [Figure 8b](#) for comparison. Because of the thermal expansion resulting from the combustion in the strut wake, the shock waves in the downstream are different from those in the non-reacting flow. By the same token, the expansion fans originating from the tips of the strut are substantially weaker, the shear layers are pushed away from the combustor centerline, and the shock waves formed by the shear layer disappear. Although the present 2D calculation reproduces these flow characteristics, it shows a narrower combustion zone in the wake, which is observed even in the previous 3D simulations of Berglund and Fureby (2007) and Fureby et al. (2014).

Time-averaged streamwise velocity profiles are shown in [Figure 9](#) and compared with the experimental results that are available only at locations A, B, and E. At location A, where the strut wake and fuel jet flow expansion dominate the velocity field, the present 2D calculation predicts a larger velocity deficit compared with the experimental data. At the further downstream locations, the streamwise velocity profiles are more uniform owing to the entrainment of high-speed main flow. Again, the good agreement between

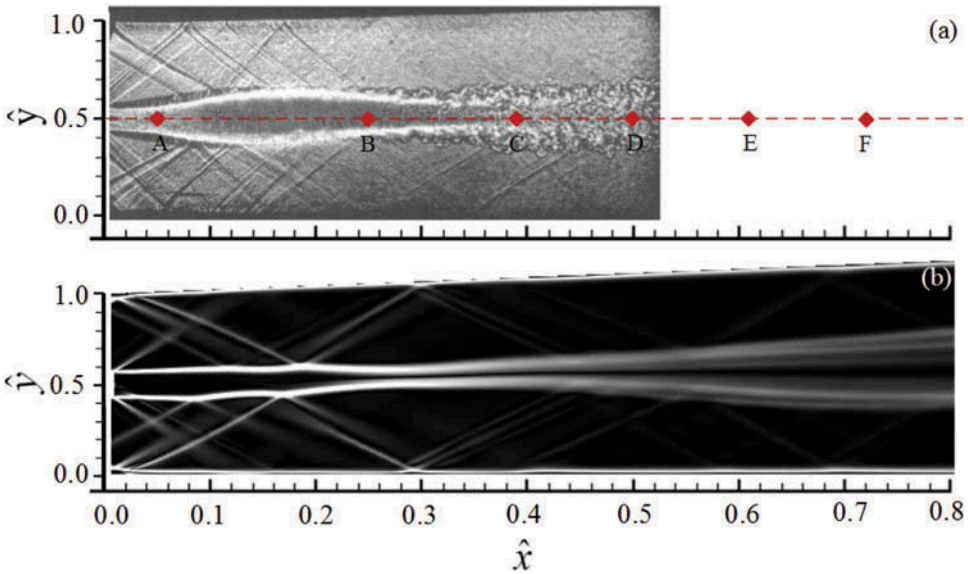


Figure 8. (a) Experimental shadow graph from Waidmann et al. (1994). (b) Time-averaged density gradient field from the 2D reacting flow calculation.

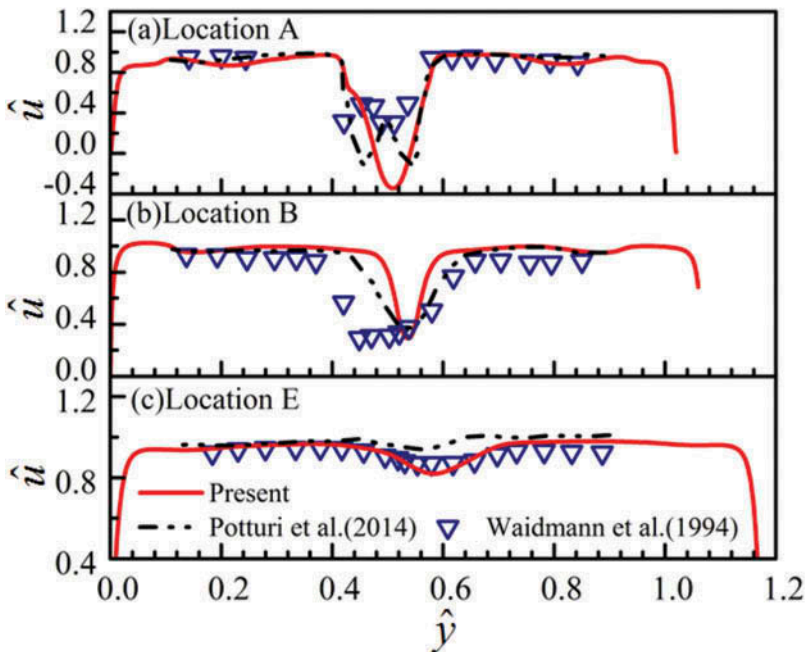


Figure 9. Time-averaged axial velocity profiles of the reacting flow at three streamwise locations.

the present 2D calculation and the experimental data implies that the 3D flow characteristics of the strut wave and fuel injection diminish rapidly in the downstream. In Figure 10, the 2D calculation for the streamwise velocity fluctuations in reacting flow

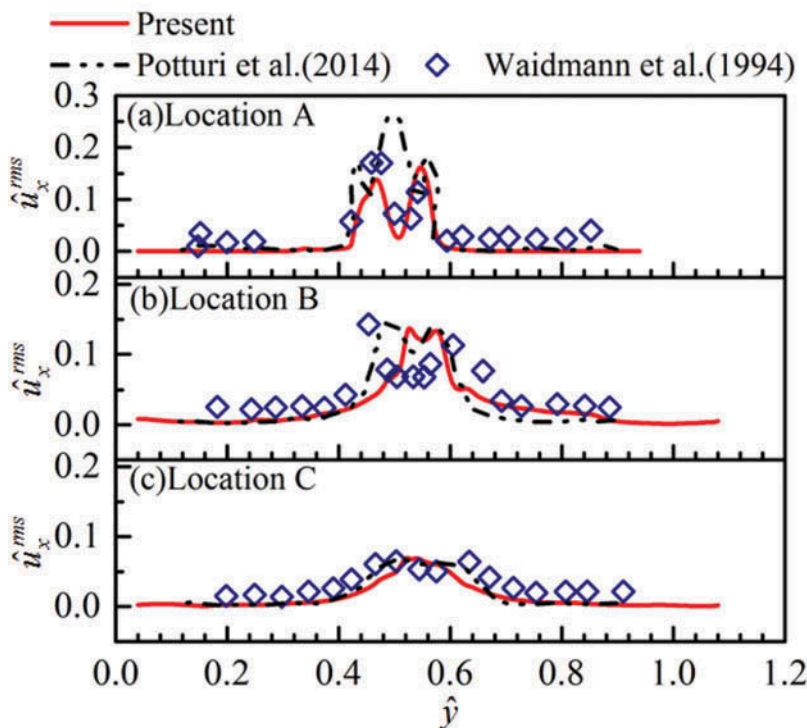


Figure 10. Streamwise velocity fluctuation profiles at three streamwise locations in the reacting flow.

show good agreement with the experimental data. It can be deduced from the velocity fluctuations that the turbulence energy k increases across the downstream region of the strut, where strut wake flow, shock wave interaction, and chemical reactions exist. Owing to the lack of more experimental data in non-reacting flow at the same streamwise locations, the contribution of the chemical reaction from the increase of turbulence fluctuations shown in the figure cannot be further differentiated.

The cross-section profiles of static temperature can be used as an overall assessment of the reacting flow simulation. As shown in Figure 11a, the temperature profile is over-predicted by the 2D calculation at location A. This result is consistent with the over-prediction of the velocity deficit in the wake at the same location, which results in a larger local Damköhler number and an earlier ignition. The temperature profile predicted by Potturi and Edwards (2014) does not, however, show a remarkable temperature raise at this location, indicating that there is no ignition and the flame is therefore detached from the strut in their simulation. It is also noted that the temperature profile predicted by Berglund and Fureby (2007) shows significant over-shooting; as such the temperature in the shear layers reaches 2200 K. At the downstream locations, the present 2D calculation shows very good agreement with the experimental data, but Potturi and Edwards's (2014) simulation shows increasing discrepancies compared with the experimental data.

It should be recognized that the present 2D LES has limitations. First, the 2D approach can significantly facilitate the computationally demanding numerical study on the DLR supersonic combustor, but it is not a general one to turbulent reacting flows that are intrinsically

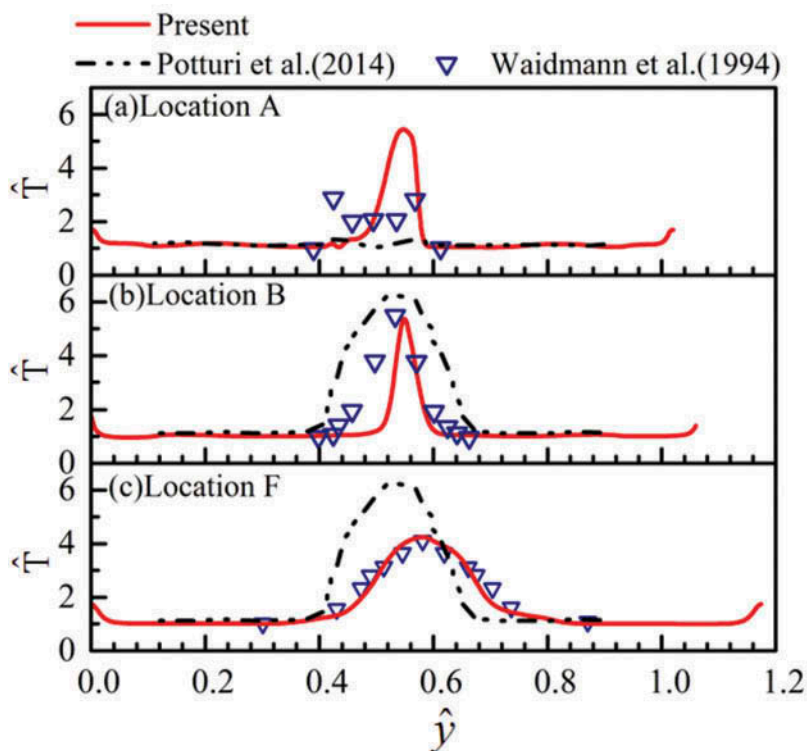


Figure 11. Time-averaged static temperature profiles of the reacting flow at three streamwise locations.

three dimensional. Second, the applicability of the 2D LES to the present problem has been verified by the 3D LES and the experiment, possibly owing to the 2D large-scale flow structures in the downstream of the strut, but it should be reexamined in the far field, where the turbulent effect in a spanwise direction may not be negligible while the experimental data are not available. Third, the present 2D LES adopts the only set of flow conditions of the DLR combustor, its application to other flow conditions, for example, to higher total temperature and larger overall equivalence ratio, needs further validations because of the possibly increased 3D flow characteristics.

Flame stabilization mechanism

To clarify the flame stabilization mechanism, we plotted various contours of static temperature and chemical species in Figure 12, from which several important observations can be made and will be discussed as follows.

First, the static temperature contour shows a small region in the strut wake as seen in Figure 12a, where the local temperature is close to the adiabatic flame temperature of the stoichiometric hydrogen/air mixture, H and OH radicals are produced, and H₂O is also found in a substantial level of concentration. This is in accordance with the experimental observation that ignition occurs in the low-speed recirculation region immediately behind the strut (Waidmann et al., 1994). Because of the asymmetric geometry of the combustion chamber, a fuel-rich zone formed in the lower part of the wake so that the reaction zone

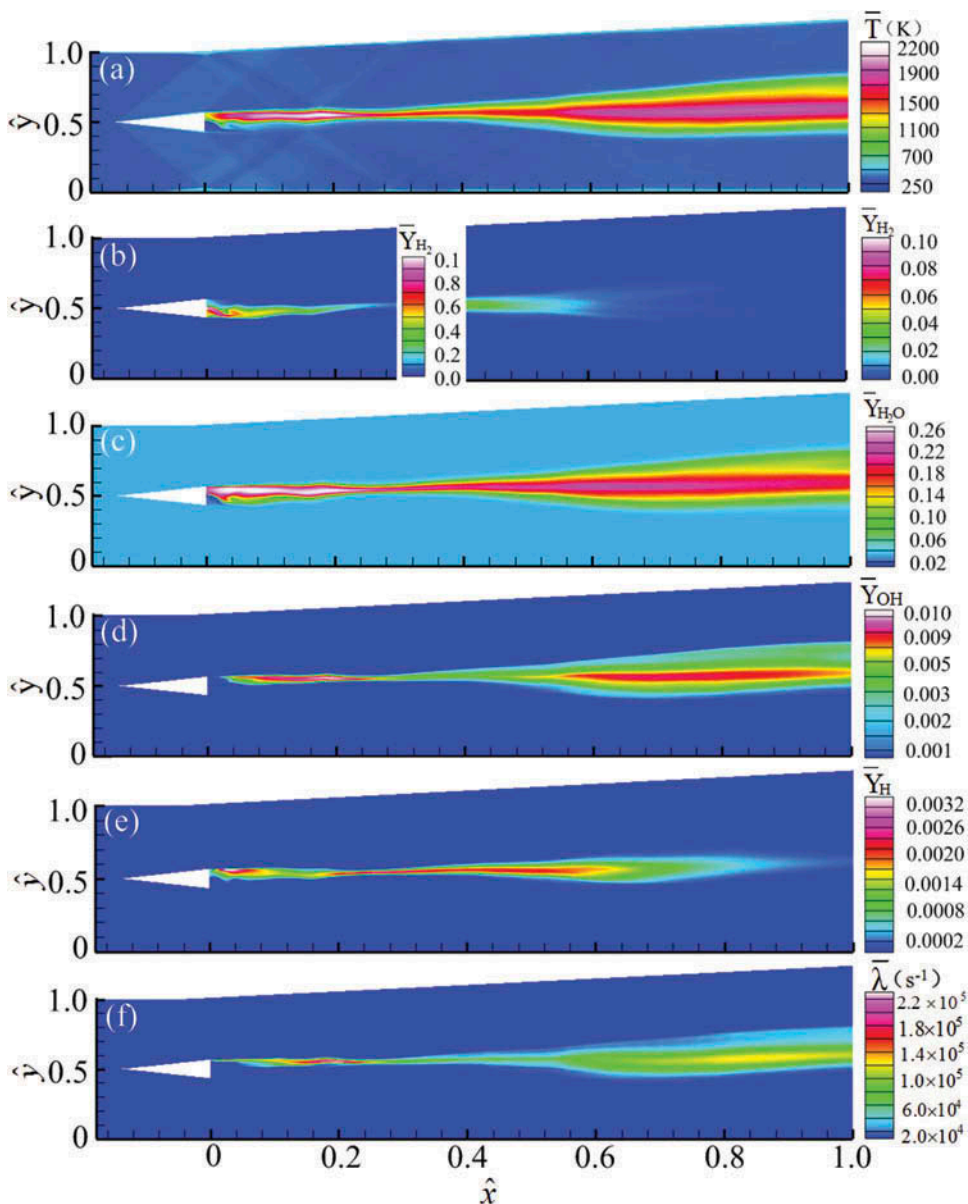


Figure 12. Contour plots of 2D reacting flow calculation using the B-9S-19R mechanism for the time-averaged (a) static temperature, (b) mass fraction of H_2 , (c) mass fraction of H_2O , (d) mass fraction of OH , (e) mass fraction of H , and (f) mixture reactivity index.

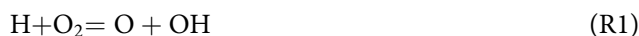
behind the strut resides only on the upper shear layer. Because heat release in this region is relatively small compared with that in the downstream, we called this region the induction stage of the DLR combustion.

Second, in the further downstream region of $0.220 < \hat{x} < 0.400$, the high-speed free-stream flow suppresses the growth of the shear layers to a very narrow region where chemical reactions seem to be inactive. Further scrutiny to [Figures 12d](#) and [12e](#) reveals that there exists

a transition stage in which $Y_{\text{H}_2\text{O}}$, Y_{OH} , and Y_{H} remain almost unchanged, migrating from the upstream to the downstream.

Third, from about $\hat{x} = 0.400$ to the exit of the combustor, intense reactions occur again owing to the active radicals transported from the upstream. It is also substantiated by a significantly enlarged high-temperature region compared with the induction stage. In the present problem, the chain-carrying reaction $\text{OH} + \text{H}_2 = \text{H}_2\text{O} + \text{H}$ is believed to contribute to the most heat release by producing water as the only stable product in the reaction system. As is shown in Figure 12c, the spatial distribution of H_2O manifests the induction, transition, and intense combustion stages.

In order to further illustrate the correlation between the flame stabilization mode and the hydrogen chain reactions, the mixture reactivity index, which was introduced by Boivin et al. (2011), is shown in Figure 12f. The mixture reactivity index quantitatively measures the competition among the below reactions for producing and consuming OH radicals:



and is hence defined by:

$$\lambda = 2k_{1f}c_{\text{O}_2}\Lambda \quad (10)$$

where

$$\Lambda = \left[(1 + 2B)^{1/2} - 1 \right] / B \quad (11)$$

$$B = 4k_{1f}c_{\text{O}_2} (k_{1f}c_{\text{O}_2} + k_{2f}c_{\text{H}_2} + k_{3f}c_{\text{H}_2}) / k_{2f}k_{3f}c_{\text{H}_2}^2 \quad (12)$$

Here k_{if} is the forward rate of the i th reaction ($i = 1, 2, 3$), and c is the molar concentration of species. Phenomenologically, the mixture reactivity index is inversely proportional to the auto-ignition time under homogeneous conditions (Boivin et al., 2012). Consequently, a large value of λ means that R1 and R2 control the reactivity of the mixture and facilitate ignition by producing OH radicals. For small λ , R3 dominantly consumes OH radicals and therefore retards ignition.

It is seen from Figure 12f that the three-stage combustion mode can be further substantiated as λ is the highest in the induction stage, substantially reduced in the transition state, and increased moderately owing to the high temperature in the intense combustion stage. It is noted that Waidmann et al. (1994) observed the similar three-stage combustion model by virtue of the spontaneous OH emission. A direct comparison between the present OH profiles with theirs is however difficult because the experimental data was obtained via integration over the chamber depth.

To further scrutinize the instantaneous characteristics of OH production and consumption, Figure 13 shows a series of instantaneous Y_{OH} contours with a time interval of 1.0×10^{-5} s. It is seen that a fluid parcel with a high Y_{OH} , denoted by P1, emerges on the fuel-rich side of the shear layer, in Figure 13a. Subsequently, P1 is advected to the downstream, while distorted by the shear stretching, but not weakened in Y_{OH} , as seen

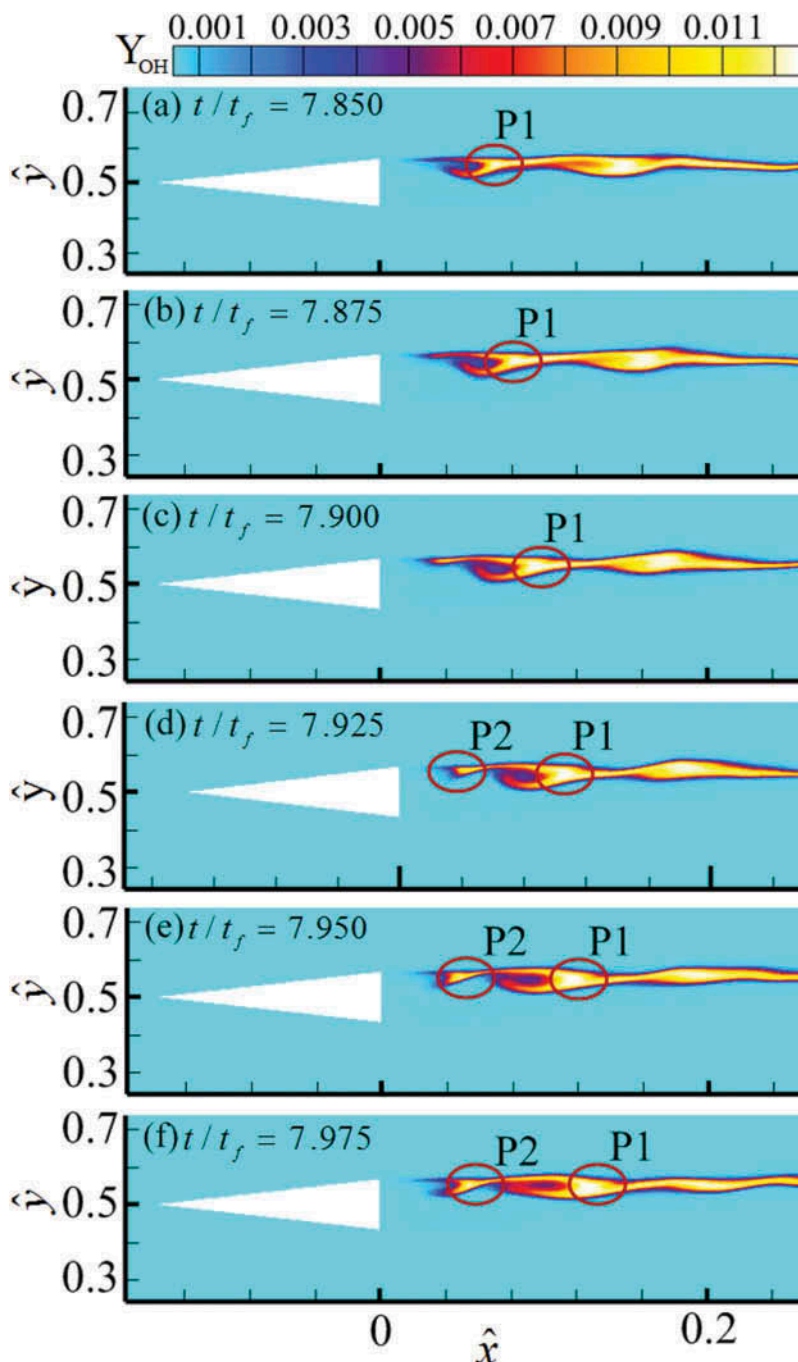


Figure 13. Time evolution of instantaneous field of OH radical mass fraction in the 2D reacting flow calculation.

in Figures 13b and 13c. A new fluid parcel with a high Y_{OH} , denoted by P2, emerges in the upstream of the shear layer, meanwhile P1 moves further downstream and eventually merges with the relatively stable shear layer. This verifies our previous conjecture that the

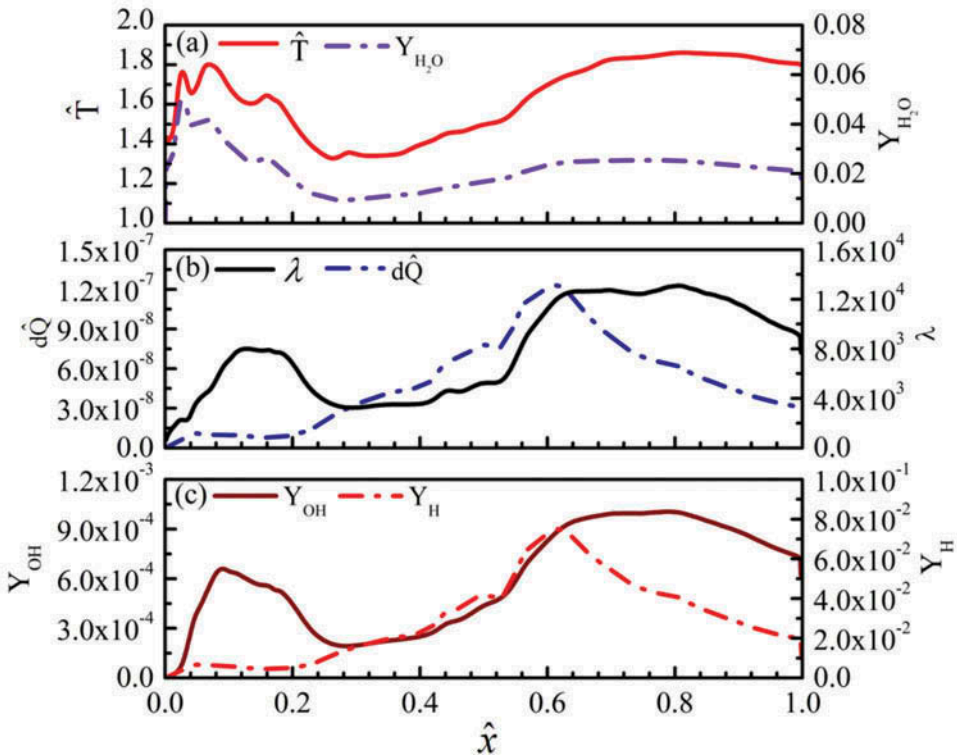


Figure 14. Pseudo-1D streamwise distributions of (a) static temperature and mass fraction of H_2O , (b) heat release rate and mixture reactivity index, and (c) mass fractions of OH and H.

intense combustion stage is sustained by the OH radicals formed in the induction stage and transported through the transition stage.

In consideration of that, quasi-1D analysis has been widely used in the configuration design and performance evaluation of supersonic combustors (Heiser and Pratt, 1994). We averaged the present 2D calculation results in the transverse direction to obtain pseudo-1D results. It is seen that the pseudo-1D temperature profile appears at two crests, one located in the immediate downstream of the strut and the other in the far downstream of the combustor, as shown in Figure 14a. The mixture reactivity index shown in Figure 14b and the mass fraction of OH shown in Figure 14c has the same non-monotonic trends. Consequently, the three-stage combustion mode can be also seen in pseudo-1D results. Another interesting observation is that most heat release occurs in the intense combustion stage so that the heat release rate profile in Figure 14b shows a slight rise in the immediate downstream of the strut but a significant increase in the far downstream.

Influence of reaction mechanisms and key reaction steps

As discussed in the Introduction, various detailed reaction mechanisms and their reduced versions with or without experimental fitting have been used in previous simulations (Cao et al., 2015; Fureby et al., 2014; Génin and Menon, 2010b; Potturi and Edwards, 2014). The argument of one mechanism exceeding over another is often based on the comparison and

sensitivity analysis on the simplified zero-dimensional or 1D laminar flame problems. Performing the sensitivity analysis of reaction mechanisms in multi-dimensional turbulent combustion problems, even though to the simplest hydrogen oxidation, is computationally formidable if not completely intractable. Nevertheless, the present 2D calculation, which demands substantially less computational resource and has been sufficiently validated in the preceding sections, enables such an analysis with the most updated hydrogen oxidation mechanism (B-9S-19R) of Burke et al. (2011).

To quantify the influence of the mechanisms with different levels of reduction, we repeated the simulation discussed in the fourth section with three mechanisms in the descending extent of mechanism reduction: M-3S-1R, E-7S-7R, and B-9S-19R. The B-9S-19R mechanism has been validated against a great number of various experimental data over wide conditions of temperature (300–3000 K) and pressure (up to 87 atm), which cover the temperature and pressure ranges of the DLR combustor. Furthermore, the B-9S-19R mechanism has been proved to be quantitatively predictable at high pressures and for the shock-wave-containing flow field (Shi et al., 2016). As for the E-7S-7R mechanism, its validated conditions are 298–2500 K for temperature and up to 7 atm for pressure. The M-3S-1R 1-step mechanism covers temperatures from 300–2000 K and pressure up to 4 atm.

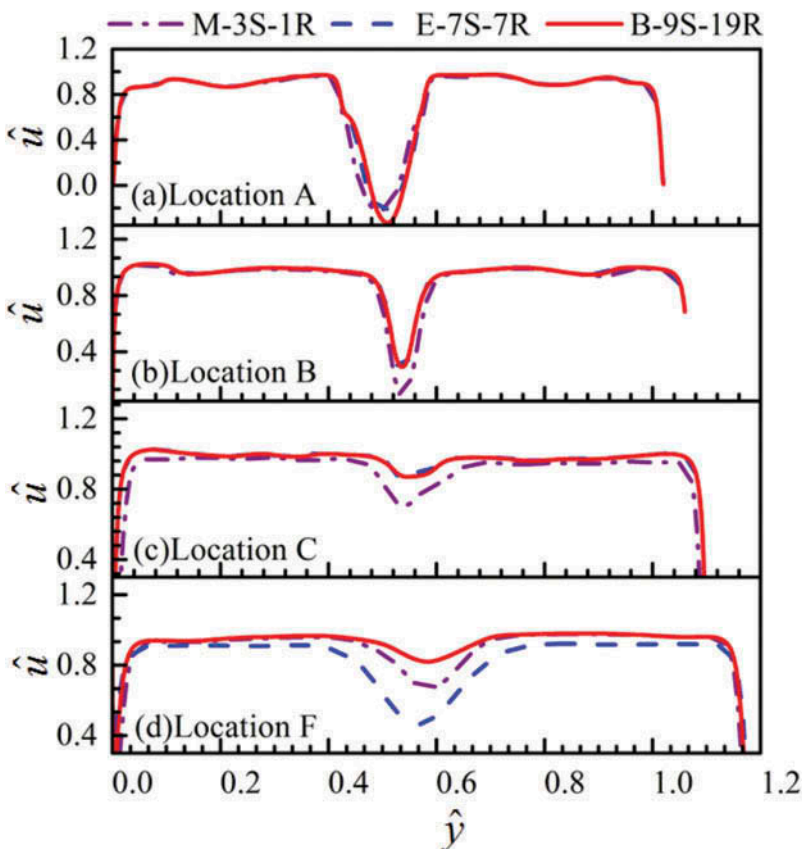


Figure 15. Time-averaged streamwise velocity profiles at four streamwise locations using three hydrogen oxidation mechanisms.

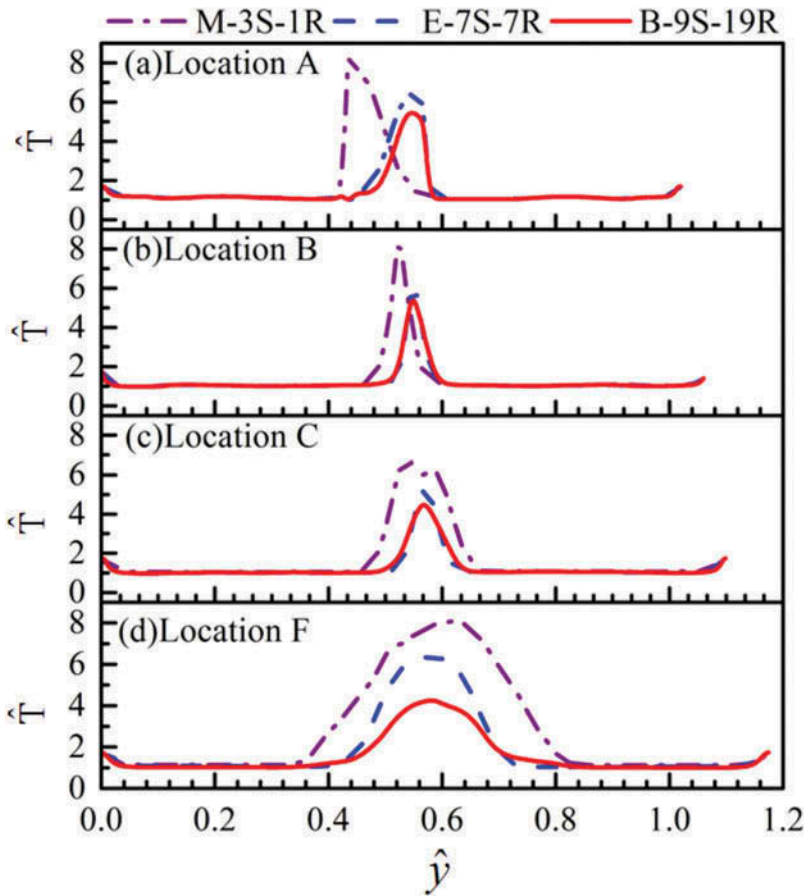


Figure 16. Time-averaged static temperature profiles at four streamwise locations using three hydrogen oxidation mechanisms.

For clarity and simplicity, the cross-section profiles of static temperature and axial velocity are shown and compared in Figures 15 and 16, respectively. As shown in Figure 15a, the velocity field in the immediate downstream of the strut is very similar for the three predictions because it is mainly controlled by the wake flow and fuel injection rather than combustion. As a matter of fact, the heat release in the induction stage is too small to make significant changes to the local flow field by thermal expansion. Significant velocity differences can be found in the further downstream locations, as shown in Figures 15b–15d, because the three mechanisms result in distinctly different heat release rates and spatial distributions, as will be elaborated shortly.

As to the three mechanism predictions to the static temperature, they have a substantial difference in the immediate downstream of the strut, as shown in Figure 16a. Because the M-3S-1R mechanism neglects all the chain reactions and predicts immediate heat release upon reaction, the temperature peak predicted by the M-3S-1R mechanism appears as an earlier, higher, and more rapid rise than do the other predictions. Comparing the E-7S-7R and the B-9S-19R mechanisms, we can see that the velocity profiles at the first three locations are almost identical and that the same trend is also observed in the temperature

profiles, as shown in Figures 15 and 16. Although the velocity and temperature profiles at location F predicted by the E-7S-7R mechanism are moderately different from those by the B-9S-19R mechanism, the E-7S-7R mechanism enables to qualitatively capture the three-stage combustion stabilization mode. The quantitative difference may be contributed to the different predictions for heat release rate.

The rate of heat release and its distribution are the crucial factors influencing the combustion performance of a supersonic combustor (Kumaran and Babu, 2009). Consequently, the quasi-1D analysis, which requires the experimentally measured static wall pressure and a heat release model for problem closure, has been always used to model supersonic combustor as a fast and qualitatively reliable tool (Heiser and Pratt, 1994; Tian et al., 2014). In this regard, the present analysis of a chemical reactions mechanism takes the heat release into account as an important measure. The different predictions of the reaction mechanisms for heat release can be clearly seen in the pseudo-1D plots in Figure 17. In contrast to the other two mechanisms, the M-3S-1R mechanism produces a rapid heat release after the induction stage that ends around $\hat{x} = 0.200$ and does not show any local heat release peak in the downstream. The heat release distribution predicted by the E-7S-7R mechanism shows the same trend with that by the B-9S-19R mechanism. In addition, the induction and transition stages predicted by the B-9S-19R mechanism are also reproduced by the E-7S-7R mechanism. Considering that the present study is focused on revealing the combustion stabilization mechanisms and that reduced mechanisms are computationally favorable compared with the detailed ones in many supersonic combustion simulations, the 7-step mechanism is regarded as a qualitatively acceptable one for studying the DLR combustor.

We can attribute the above findings to the key chain reactions, R1–R3, that are included in both mechanisms. These key reactions are identified based on the following reasons. First, in the study of Boivin et al. (2011, 2012), R1, R2, and R3 are proven to be essential for the reactivity of the hydrogen-air combustion system. Second, by virtue of our sensitivity studies of auto-ignition and flame propagating problem under the DLR operating conditions (refer to the supporting materials). Third, one of the important findings in the fourth section of the present study is the three-stage combustion stabilization, in which the generation, migration,

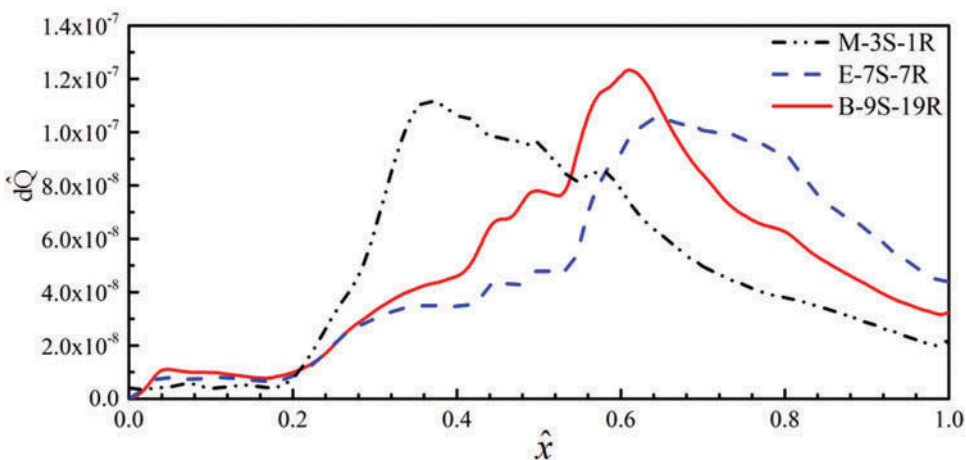


Figure 17. Pseudo-1D streamwise distribution of heat release rate calculated by using three mechanisms.

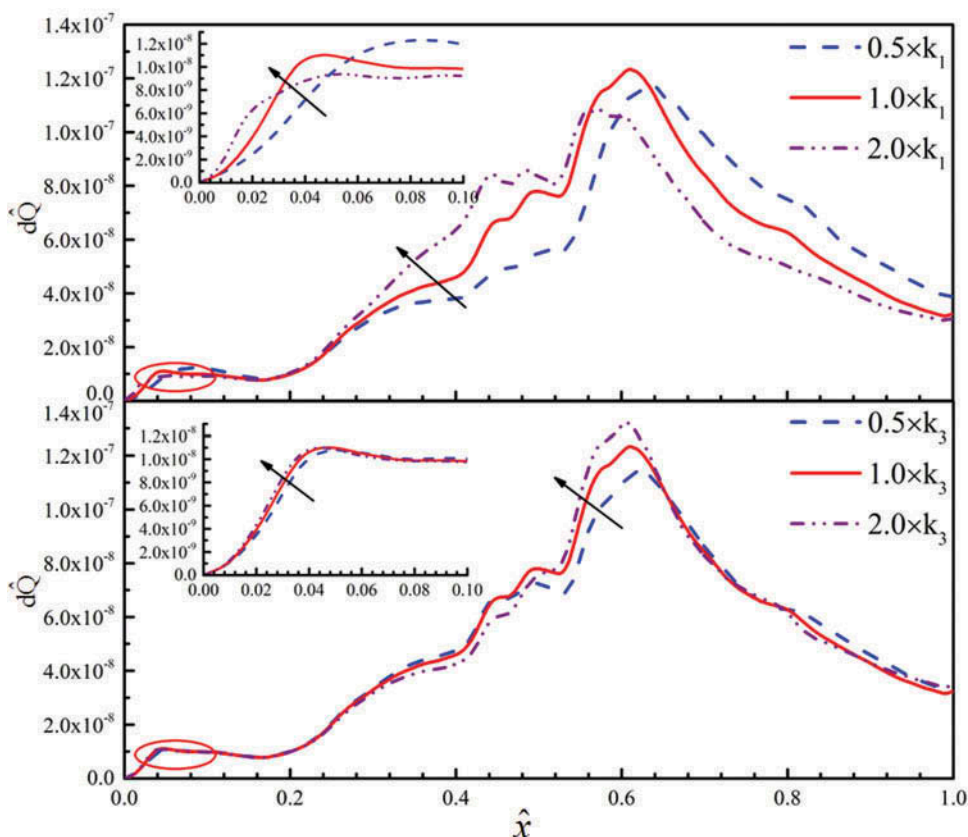


Figure 18. Pseudo-1D streamwise heat release distribution calculated by using the B-9S-19R mechanism with (a) sensitivity analysis of R1 and (b) sensitivity analysis of R3.

and consumption of active radicals, such as H, OH, and O, play a crucial role. R1, R2, and R3 are the controlling reactions for these radicals.

By using the B-9S-19R mechanism, we analyzed the sensitivity of the pseudo-1D heat release distribution to the reactions rates of R1 and R3 by perturbing (either doubling or halving) their rate constants, as shown in Figure 18. It is seen that the perturbations imposed to the rate of R1 lead to a significant difference in the induction and intense combustion stages, implying that R1 is crucial in these stages for producing or consuming radicals. The perturbations imposed to the rate of R3, which is responsible for the most heat release, reveal a negligible difference in the induction stage but significant difference in the intense combustion stage. This can be understood because the relatively low concentration of OH radicals in the induction stage results in the small rate of R3, which is in turn insensitive to the perturbations to R3, as shown in Figure 18b. In the intense combustion stage, R3 dominates the heat release rate and therefore is sensitive to any perturbations to its rate constants. As a result, the E-7S-7R and B-9S-19R mechanisms that have different rate constants for R3 produce moderately different heat release rates, which affect their predictions to the velocity and temperature profiles in the intense combustion stage.

Concluding remarks

In the present study, numerical investigation of the flame stabilization mode of the DLR hydrogen fueled strut injection model combustor was carried out by using an in-house LES code based on the OpenFoam platform. In order to facilitate the sensitivity analysis of detailed reaction mechanism of hydrogen combustion in the LES, a 2D model was proposed to maintain the global equivalence ratio and it has been sufficiently validated against both the 3D simulation and the available experimental data; meanwhile its limitations are fully recognized. Experimental validations have conducted for both non-reacting and reacting flows and overall good agreements have been obtained between experiment and simulation regarding the velocity and temperature profiles. By virtue of the flow visualization of temperature and species concentration and of the pseudo 1D analysis of heat release rate, a three-stage flame stabilization mode consisting of the induction, transition, and intense combustion stage, has been proposed and substantiated. From the comparison of three hydrogen oxidation mechanisms of different levels of reduction, the important role of key chain reactions in correctly reproducing the flame stabilization mode has been clarified. Specifically, the chain-carrying reactions to produce OH radicals is indispensable in the induction stage as well as in the intense combustion stage; the water production reaction that consumes OH radicals is less important in the induction stage than in the intense combustion stage, where the most heat release occurs.

Acknowledgment

The authors are grateful to the National Supercomputer Centre in Tianjin for computational resource.

Funding

The work at the Hong Kong Polytechnic University was supported by the Hong Kong RGC/GRF (PloyU 152651/16E) and in part by the SRFDP & RGC ERG Joint Research Scheme (M-PolyU509/13), while work at the Institute of Mechanics was supported by the National Natural Science Foundation of China (Grant No. 11502270) and Training Program of the Major Research Plan of the National Natural Science Foundation of China (Grant No. 91641110).

References

- Baba-Ahmadi, M.H., and Tabor, G. 2009. Inlet conditions for LES using mapping and feedback control. *Comput. Fluids.*, **38**(6), 1299–1311.
- Balaras, E., Benocci, C., and Piomelli, U. 1996. Two-layer approximate boundary conditions for large-eddy simulations. *AIAA J.*, **34**(6), 1111–1119.
- Baurle, R.A., Alexopoulos, G.A., and Hassan, H.A. 1994. Assumed joint probability density function approach for supersonic turbulent combustion. *J. Propul. Power.*, **10**(4), 473–484.
- Ben-Yakar, A., Mungal, M.A., and Hanson, R.K. 2006. Time evolution and mixing characteristics of hydrogen and ethylene transverse jets in supersonic crossflows. *Phys. Fluids*, **18**(2), 026101.
- Berglund, M., and Fureby, C. 2007. LES of supersonic combustion in a scramjet engine model. *Proc. Combust. Inst.*, **31**(2), 2497–2504.
- Bertin, J.J., and Cummings, R.M. 2003. Fifty years of hypersonics: Where we've been, where we're going. *Prog. Aerosp. Sci.*, **39**(6–7), 511–536.

- Boivin, P., Dauptain, A., Jiménez, C., and Cuenot, B. 2012. Simulation of a supersonic hydrogen–air autoignition-stabilized flame using reduced chemistry. *Combust. Flame*, **159**(4), 1779–1790.
- Boivin, P., Jiménez, C., Sánchez, A.L., and Williams, F.A. 2011. An explicit reduced mechanism for H₂–air combustion. *Proc. Combust. Inst.*, **33**(1), 517–523.
- Burke, M.P., Chaos, M., Ju, Y., Dryer, F.L., and Klippenstein, S.J. 2011. Comprehensive H₂/O₂ kinetic model for high-pressure combustion. *Int. J. Chem. Kinet.*, **44**(7), 444–474.
- Cao, C., Ye, T., and Zhao, M. 2015. Large eddy simulation of hydrogen/air scramjet combustion using tabulated thermo-chemistry approach. *Chin. J. Aeronaut.*, **28**(5), 1316–1327.
- Cecere, D., Ingenito, A., Giacomazzi, E., Romagnosi, L., and Bruno, C. 2011. Hydrogen/air supersonic combustion for future hypersonic vehicles. *Int. J. Hydrogen Energy*, **36**(18), 11969–11984.
- Chakravarthy, V.K., and Menon, S. 2001. Large-eddy simulation of turbulent premixed flames in the flamelet regime. *Combust. Sci. Technol.*, **162**(1), 175–222.
- Chase, J. L., M. W., Curnutt, A. T., Hu, H., Prophet, A. N., Syverud and L. C. Walker. 1974. JANAF thermochemical Tables, 1974 Supplement.. *J. Phys. Chem. Ref. Data*, **3**(2), 311–480.
- Davidenko, I.G.D., and Magre, P. 2003. Numerical simulation of hydrogen supersonic combustion and validation of computational approach. Presented at the 12th AIAA International Space Planes and Hypersonic Systems and Technologies Conference, Norfolk, VA, December 15–19.
- Eklund, D.R., Drummond, J.P., and Hassan, H.A. 1990. Calculation of supersonic turbulent reacting coaxial jets. *AIAA J.*, **28**(9), 1633–1641.
- Fulton, J.A., Edwards, J.R., Cutler, A., McDaniel, J., and Goyne, C. 2016. Turbulence/chemistry interactions in a ramp-stabilized supersonic hydrogen–air diffusion flame. *Combust. Flame*, **174**, 152–165.
- Fureby, C. 2012. LES for supersonic combustion. Presented at the 18th AIAA/3AF International Space Planes and Hypersonic Systems and Technologies Conference, Tours, France, September 24–28.
- Fureby, C., Alin, N., Wikström, N., Menon, S., Svanstedt, N., and Persson, L. 2004. Large eddy simulation of high-Reynolds-number wall bounded flows. *AIAA J.*, **42**(3), 457–468.
- Fureby, C., Chapuis, M., Fedina, E., and Karl, S. 2011. CFD analysis of the HyShot II scramjet combustor. *Proc. Combust. Inst.*, **33**(2), 2399–2405.
- Fureby, C., Fedina, E., and Tegnér, J. 2014. A computational study of supersonic combustion behind a wedge-shaped flameholder. *Shock Waves*, **24**(1), 41–50.
- Fureby, C., Gosman, A., Tabor, G., Weller, H., Sandham, N., and Wolfshtein, M. 1997. Large eddy simulation of turbulent channel flows. *Turbul. Shear Flows*, **11**, 28–33.
- Génin, F., and Menon, S. 2010a. Dynamics of sonic jet injection into supersonic crossflow. *J. Turbul.*, **11**, N4.
- Génin, F., and Menon, S. 2010b. Simulation of turbulent mixing behind a strut injector in supersonic flow. *AIAA J.*, **48**(3), 526–539.
- Gong, C., Jangi, M., Bai, X.-S., Liang, J.-H., and Sun, M.-B. 2017. Large eddy simulation of hydrogen combustion in supersonic flows using an Eulerian stochastic fields method. *Int. J. Hydrogen Energy*, **42**(2), 1264–1275.
- Greenshields, C.J., Weller, H.G., Gasparini, L., and Reese, J.M. 2009. Implementation of semi-discrete, non-staggered central schemes in a colocated, polyhedral, finite volume framework, for high-speed viscous flows. *Int. J. Numer. Methods Fluids*, **63**(1), 1–21.
- Heiser, W.H., and Pratt, D.T. 1994. *Hypersonic Airbreathing Propulsion*, Washington D C, AIAA Education.
- Huang, Z.-W., He, G.-Q., Qin, F., and Wei, X.-G. 2015. Large eddy simulation of flame structure and combustion mode in a hydrogen fueled supersonic combustor. *Int. J. Hydrogen Energy* **40** (31), 9815–9824.
- Jachimowski, C.J. 1988. An analytical study of the hydrogen-air reaction mechanism with application to scramjet combustion. Report NASA-TP-2791.
- Karlsson, A. 1995. Modeling auto-ignition, flame propagation and combustion in non-stationary turbulent sprays. PhD. Chalmers University of Technology, Gothenburg, Sweden.
- Kumaran, K., and Babu, V. 2009. Investigation of the effect of chemistry models on the numerical predictions of the supersonic combustion of hydrogen. *Combust. Flame*, **156**(4), 826–841.

- Kurganov, A., and Tadmor, E. 2000. New high-resolution central schemes for nonlinear conservation laws and convection–diffusion equations. *J. Comput. Phys.*, **160**(1), 241–282.
- Li, J., Zhang, L., Choi, J.Y., Yang, V., and Lin, K.-C. 2014a. Ignition transients in a scramjet engine with air throttling. Part I: Nonreacting flow. *J. Propul. Power*, **30**(2), 438–448.
- Li, J., Zhang, L., Choi, J.Y., Yang, V., and Lin, K.-C. 2014b. Ignition transients in a scramjet engine with air throttling. Part II: Reacting flow. *J. Propul. Power*, **31**(1), 79–88.
- Li, X., Wu, K., Yao, W., and Fan, X. 2016a. A comparative study of highly underexpanded nitrogen and hydrogen jets using large eddy simulation. *Int. J. Hydrogen Energy*, **41**(9), 5151–5161.
- Li, X., Yao, W., and Fan, X. 2016b. Large-eddy simulation of time evolution and instability of highly underexpanded sonic jets. *AIAA J.*, **54**(10), 3191–3211.
- Marinov, N., Westbrook, C., and Pitz, W. 1995. Detailed and global chemical kinetics model for hydrogen. Presented at the 8th International Symposium on Transport Properties, July 16–20, 1995, San Francisco, California.
- Nordin-Bates, K., Fureby, C., Karl, S., and Hannemann, K. 2017. Understanding scramjet combustion using LES of the HyShot II combustor. *Proc. Combust. Inst.*, **36**(2), 2893–2900.
- Oevermann, M. 2000. Numerical investigation of turbulent hydrogen combustion in a SCRAMJET using flamelet modeling. *Aerosp. Sci. Technol.*, **4**(7), 463–480.
- Pino Martín, M., Piomelli, U., and Candler, G.V. 2000. Subgrid-scale models for compressible large-eddy simulations. *Theor. Comput. Fluid Dyn.*, **13**(5), 361–376.
- Potturi, A.S., and Edwards, J.R. 2012. LES/RANS simulation of a supersonic combustion experiment. Presented at the 50th AIAA Aerospace Sciences Meeting including the New Horizons Forum and Aerospace Exposition, Nashville, TN, January 9–12.
- Potturi, A.S., and Edwards, J.R. 2014. Hybrid large-eddy/Reynolds-averaged Navier–Stokes simulations of flow through a model scramjet. *AIAA J.*, **52**(7), 1417–1429.
- Rogers, R.C., and Chinitz, W. 1983. Using a global hydrogen-air combustion model in turbulent reacting flow calculations. *AIAA J.*, **21**(4), 586–592.
- Shi, L., Shen, H., Zhang, P., Zhang, D., and Wen, C. 2016. Assessment of vibrational non-equilibrium effect on detonation cell size. *Combust. Sci. Technol.*, **189**(5), 841–853.
- Tian, L., Chen, L., Chen, Q., Li, F., and Chang, X. 2014. Quasi-one-dimensional multimodes analysis for dual-mode scramjet. *J. Propul. Power*, **30**(6), 1559–1567.
- Waidmann, W., Alff, F., Böhm, M., Brummund, U., Clauß, W., and Oswald, M. 1994. Supersonic combustion of hydrogen/air in a scramjet combustion chamber. *Space Technol.*, **15**(6), 421–429.
- Yoshizawa, A. 1986. Statistical theory for compressible turbulent shear flows, with the application to subgrid modeling. *Phys. Fluids*, **29**(7), 2152–2164.